Journal of Energy Storage 49 (2022) 104135

Contents lists available at ScienceDirect

Journal of Energy Storage

journal homepage: www.elsevier.com/locate/est

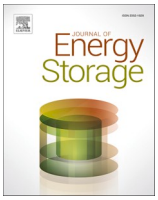

Research Papers

Serpentine flow field with changing rib width for enhancing electrolyte penetration uniformity in redox flow batteries

Jie Sun [a,b], Baichen Liu [a,1], Menglian Zheng [a,c,*], Yansong Luo [a], Zitao Yu [a,c]

[a] Institute of Thermal Science and Power Systems, School of Energy Engineering, Zhejiang University, Hangzhou, 310027, China
[b] Institute of Energy and Environment Engineering, NingboTech University, Ningbo, 315100, China
[c] State Key Laboratory of Clean Energy Utilization, School of Energy Engineering, Zhejiang University, Zheda Road 38, Hangzhou, 310027, China

ARTICLE INFO

Keywords:
VRFB
Serpentine flow field
Electrolyte penetration
Concentration distribution uniformity
Mass transfer enhancement
Concentration overpotential

ABSTRACT

It has been largely agreed that the electrolyte penetration is mainly driven by the pressure gradient between two neighboring flow passages in the serpentine flow field. The present study proposes to modify the distribution of the under-the-rib hydraulic resistance for making it in concert with the pressure gradient and thereby ameliorating the distribution uniformity of the volumetric electrolyte flow penetrating into the interface between the serpentine flow field and the porous carbon electrode. Three modified serpentine flow field designs are devised based on the conventional serpentine flow field by changing the width of the ribs in three distinct manners, including serpentine flow field with the sloping channels, serpentine flow field with the partially sloping channels, and serpentine flow field with the stepwise channels. The experimental results show that by using the modified serpentine flow fields, the limiting current density of the small-scale flow cell (active area corresponding to 5 cm × 5 cm) is improved by up to 60% of that of the flow cell with the conventional serpentine flow field. The simulative results show that the impacts of the proposed designs on the electrolyte penetration uniformity is expected to be more significant in large-scale flow cells. And the effectiveness of the modified serpentine flow fields is subject to the magnitude of the under-the-rib hydraulic resistance and the applied flow rate.

1. Introduction

Energy storage technologies are expected to play critical roles in improving the reliability and stability of energy supply in future's energy systems with a high penetration of intermittent renewables [1]. Redox flow batteries (RFBs) are ones of the most promising energy storage technologies because of the benefits associated with their intrinsically decoupled energy and power configurations [2,3]. Although the decoupled structure increases the flexibility of the RFB system, it brings about new challenges when the positive/negative electrolyte circulates between the positive/negative tank and the battery stack [4]. For example, in practical applications, the massive pump loss cuts down the energy efficiency of the RFB system by more than 5% [5,6]. Besides, the nonuniform delivery of reactants within the porous electrode is usually the limiting factor for the applied current and power density per active area of the electrode [7,8], especially for large-scale flow cells [9]. Recognizing that under a given power capacity, an enhancement in the peak power density effectively reduces the amount of essential materials required in a RFB stack, such as bipolar plate, porous carbon material, and ion-selective membrane, a further reduction in the RFB cost calls for a substantial improvement in terms of mass transfer capability [10,11]. To resolve above issues, diverse flow fields are introduced into the RFBs. In principle, flow fields not only cut down the electrolyte pressure drop by shortening the electrolyte flow path in the electrode, but also improve the distribution uniformity of the reactants within the whole electrode [12,13].

In the early stage, most of the flow field designs in the RFBs were inspired by the flow fields implemented in the fuel cells, such as parallel flow field [14], serpentine flow field (SFF) [15], and interdigitated flow field (IFF) [16]. Over the last few years, as one of the widely used flow fields, the SFF has been verified extensively via experimental and simulative approaches that it could effectively enhance the mass transfer of the reactants within RFBs [17–19]. The SFF is devised with one serpentine channel connecting the inlet and outlet of the flow cell (as

* Corresponding author.
E-mail address: menglian_zheng@zju.edu.cn (M. Zheng).
[1] Co-first author

https://doi.org/10.1016/j.est.2022.104135
Received 30 September 2021; Received in revised form 29 December 2021; Accepted 29 January 2022
Available online 15 February 2022

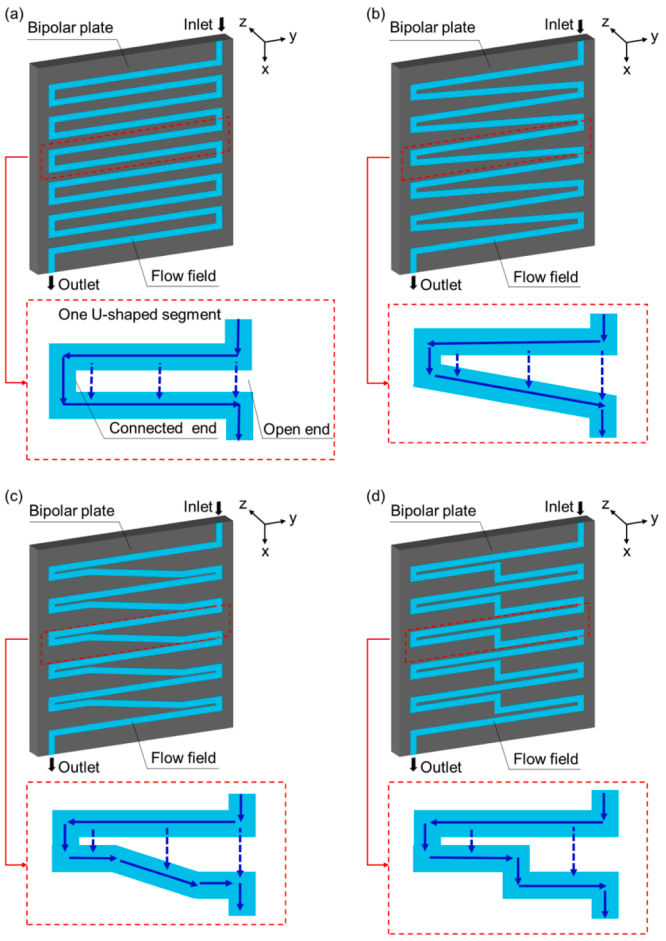

Fig. 1. Schematics of (a) conventional serpentine flow field, (b) serpentine flow field with the sloping channels, (c) serpentine flow field with the partially sloping channels, and (d) serpentine flow field with the stepwise channels. Figures are not plotted to the scale. The blue solid and dashed lines indicate the electrolyte flow paths in the channel and in the under-the-rib electrode, respectively.

shown in Fig. 1). Although the serpentine channel effectively enhances the mass transfer of the reactants within the porous electrode, there is no guarantee of the complete electrolyte penetration beneath the landings/ribs, which is distinct from the penetration pattern in the flow cell with the IFF or in the "flow-through" flow cell [20]. The uncertainty with respect to the amount and distribution of the electrolyte that penetrates into the electrode has been one of the major challenges that constrains the further improvement of the SFF designs [21].

A few previous studies have explored the underlying mechanisms for the electrolyte penetration in the flow cell with the SFF. As seen in Fig. 1a, in the SFF, each pair of two adjacent parallel flow passages and the corner channel connecting them jointly form a U-shaped segment. It has been largely agreed in previous studies that the primary driving force for electrolyte by-passing the electrode is associated with the relatively magnitude of the hydraulic resistance of the porous electrode to the resistance between the parallel flow passages [22–25]. When the former is less, a portion of the electrolyte is driven into the porous electrode through the edge of one flow passage where the pressure is relatively high, then flows through the porous electrode, and finally flows out of the electrode along the downstream adjacent flow passage where the pressure is relatively low, forming the so-called under-the-rib flow or intra-electrode flow. To this end, the design and operation parameters that affect the local pressure distribution and under-the-rib hydraulic resistance jointly determine the velocity magnitude and distribution of the intra-electrode flow in the flow cell with the SFF. For instance, Ke et al. performed a series of numerical simulations to explore how the electrode properties (such as porosity, thickness, and permeability) affected the intra-electrode flow of the electrolyte. Their results showed significant enhancements in the electrolyte penetration at the flow field-porous electrode interface with the increasing porosity, permeability, and thickness of the electrode, as these changes reduced the under-the-rib hydraulic resistance of the electrode [23,26]. Besides, Houser et al. experimentally found that the increment in the number of carbon paper layers assembled in one flow cell had higher positive impacts on the cell with the SFF in terms of the effective capacity and voltage efficiency as compared to that with the IFF [27]. The authors attributed the relatively high efficiency gain to the influential improvement in the electrolyte penetration amount when the SFF was applied [27]. The similar trend was also observed by Maurya et al. that the performance of the SFF was more sensitive to the electrode property, particularly porosity and thickness, and the applied volumetric inlet flow rate than the IFF [28].

In addition to the electrolyte penetration amount, the nonuniform penetration distribution is also a critical issue that the flow cell implemented with the SFF faces with. To get a deep understanding of the distribution of the electrolyte penetration guided by the SFF, Zhang et al. developed a lumped parameter model for one U-shaped segment of the SFF, based on which the volumetric penetration distribution was estimated [24]. The authors found that the pressure difference between the two parallel flow passages exhibited a declining trend from the open to connected end of the U-shaped segment (see Fig. 1a), leading to a larger amount of electrolyte being driven into the porous electrode far away from the corner compared to that close to the conner turn [24]. Besides, Ke et al. also obtained simulative results regarding the electrolyte penetration distribution in the flow cell with the SFF [25], which were consistent with the trend as shown in [24]. Although the trend has been understood and investigated via the simulative approach, the penetration distribution was more difficult to be directly visualized through experiments. Houser et al. visualized the current density distribution in the flow cell with the SFF through the printed circuit board being attached to the bipolar plate [27,29]. Considering that the galvanical hotspots on the electrode indicated the active reaction and high electrolyte velocity and thereby high electrolyte penetration amount, the authors verified that more electrolyte penetrated into the electrode beneath the neighboring channels far away from the conner turns rather than the electrode beneath the turns connecting the flow passages [27, 29].

Although the design principles for the SFF and underlying mechanisms for driving the electrolyte penetration into the electrode in the RFBs have been extensively investigated in the previous studies, few of them have attempted to address the penetration nonuniformity issue associated with the use of the SFF. Based on the understanding that the electrolyte penetration is mainly driven by the relatively magnitude of the pressure gradient between two neighboring flow passages to the under-the-rib hydraulic resistance, it is inferred that the distribution of the under-the-rib hydraulic resistance in concert with the pressure gradient may ameliorate the distribution uniformity of the electrolyte penetration, and thereby the intra-electrode velocity, in the electrode with the SFF. Therefore, in the present study, we propose to adjust the under-the-rib resistance by changing the rib width between each pair of the flow passages to improve the electrolyte penetration uniformity. Three SFF designs are proposed based on the traditional SFF as illustrated in Fig. 1. The rib widths are changed in three distinct manners, including (i) SFF with the sloping channels (termed as S-SFF in the present study; see Fig. 1b), (ii) SFF with the partially sloping channels (PS-SFF; see Fig. 1c), and (iii) SFF with the stepwise channels (SW-SFF, Fig. 1d). Details are presented in *Section 2.1*.

The rest of the paper is organized as follows. First, the design details of the proposed modified SFFs and corresponding experimental and numerical setups are elaborated in *Section 2*. Then, the resulting electrochemical and hydraulic performance of the vanadium-based RFB cell

(VRFB) with the modified SFFs and the conventional SFF are explored and compared vis-à-vis in *Section 3*. The investigated performances include the resulting polarization, charge-discharge capacity, pressure drop, and electrolyte penetration distribution. The effects of the applied flow rate and the thickness of the electrode on the polarization of the flow cell with different SFFs are also discussed in this section. Last, limitations and future work for further improvement are presented in *Section 4*. And *Section 5* concludes the paper.

2. Experimental and Computational

2.1. Serpentine flow field designs

The mismatches between the constant under-the-rib flow resistance and the varying pressure gradient that drives the intra-electrode flow of the electrolyte lead to the nonuniform distribution of the intra-electrode flow rate and thus reactants in the electrode. As the electrolyte pressure is reduced gradually when the electrolyte flows along the serpentine channel from the inlet to outlet, the pressure gradient between two neighboring channels rises gradually from the corner turn that connects the two flow passages to the open end far away from the corner turn. Therefore, changing the under-the-rib flow resistance accordingly may improve the uniformity of the electrolyte penetration at the interface between the flow passages and the porous electrode. Note that the electrolyte is also driven into the porous electrode at the interface between the corner channel and the electrode by the disturbances. Nevertheless, the penetration magnitude is significantly lower than (e.g., by a factor of 100 [25]) that driven by the pressure gradient between neighboring flow passages. Therefore, the focus of the present study is placed on the intra-electrode flow driven by the pressure gradient between two neighboring flow passages while the potential effects of the proposed SFF designs on the disturbances are regarded as out of scope of the present study. Three design principles for adjusting the under-the-rib flow resistance are proposed as follows: First, a SFF design is devised such that the width of the rib between two adjacent channels varies gradually from the connected end to the open end of each U-shaped segment. This SFF design is illustrated in Fig. 1b and termed as S-SFF (short for SFF with the sloping channels). Second, each U-shaped segment is divided into three parts equally. Only the middle part undergoes a linear change in the rib width while the width of the ribs in the other two parts keep unchanged. This design is termed as PS-SFF (short for the SFF with the partially sloping channels) and illustrated in Fig. 1c. Under the third design (see Fig. 1d; termed as SW-SFF, short for SFF with the stepwise channels), the rib width of the half length of the U-shaped segment near the open end is enlarged while the width of the other half part is reduced. To be noticed, although the width of the rib near the connected end of the U-shaped segment is narrowed to varying degrees in the rib-width-changing SFFs, the width of the rib near the open end is oppositely enlarged in the rib-width-changing SFFs. For comparison purposes, the conventional SFF with the constant width corresponding to the ribs between each pair of the adjacent channels (as illustrated in Fig. 1a) is also investigated in the present study. The total numbers of the flow passages and conner turns are same for the present four SFFs. The total lengths of the flow channels are around the same value for the three modified SFFs, with discrepancies within 1% of that in the conventional SFF. The figures of the processed bipolar plates with the investigated four SFFs for the experiments are showed in Fig. S1 and the detailed geometric parameters for the four SFFs are presented in Table S3 in *Supplementary Material*.

2.2. Experimental setups

The galvanostatic cycle tests, polarization tests, and pressure drop tests are conducted upon a VRFB flow cell for exploring the effects of the SFF designs on the electrochemical and hydraulic performance of the flow cell. The VRFB flow cell is assembled with an ion-selective membrane, two carbon-paper-based electrodes, bipolar plates, current collectors, and end plates. Sets of bipolar plates engraved with the present four SFFs (see Fig. S1 in *Supplementary Material*) are placed within the cell, respectively, during the experiments. All the tests are conducted under the nitrogen environment to avoid the oxidation of the ion V^{2+}. The environmental temperature is controlled to be constant at 25 °C.

In the flow cell system, the positive and negative electrolytes containing 1.6 mol•L^{-1} vanadium ion and 4 mol•L^{-1} sulfuric acid solution (Dalian Borong New Material Company) are pumped from the positive and negative tanks to the cell through two peristaltic pumps (Masterflex Group), respectively. Within the cell, the Nafion® 117 membrane is adopted to separate the positive and negative electrodes. Carbon paper (SIGRACET® GDL 38AA, provided by SGL Carbon) with the area corresponding to 5 cm × 5 cm is used as the electrode material. The original thickness of one-layer carbon paper is approximately 280 μm, and the electrodes consisting of multi-layer carbon papers (1 layer, 3 layers, or 5 layers; see *Section 3.4*) are adopted in the experiments. The compression rate of the electrode (defined as the ratio of the electrode thickness after compression to the original thickness in the present study) is set to be constant at approximately 70%. The PTFE flow frames are adopted to control the compression rate. The flow fields are engraved on the graphite bipolar plates (Beijing Jinglong Special Carbon Company).

During the electrochemical experiments, the Bio-Logic VSP electrochemical workstation is programmed under the given parameters and procedures as follows. The charge-discharge curves of the flow cell with the four SFFs as illustrated in Fig. 1 are obtained by conducting the galvanostatic cycle tests. The cut-off limits of the upper and lower voltages are selected as 1.8 V and 0.8 V, respectively, to prevent the over (dis-)charge of the electrolyte and the potential side reaction. The applied current density is set as 100 mA•cm^{-2} (the applied current corresponding to 2.5 A according to the active area of 25 cm^2), and the flow rate is selected as 30 mL•min^{-1}. The initial electrolyte volume stored in the positive (negative) tank is 50 mL. All the charge-discharge curves are obtained from the second cycle of two consecutive charge-discharge cycles.

The linear sweep voltammetry method is adopted for obtaining the polarization curves. The polarization experiments are conducted under the four-tank VRFB set up design (the positive and negative electrolytes both have two tanks that connect to the inlet and outlet of the flow cell, respectively [30]) to ensure that the concentration of the electrolyte entering the cell remains constant. Before the polarization tests, the state of charge (SOC) of the electrolyte is pre-charged to 0.5, with the open circuit voltage corresponding to 1.408 V. The scan voltage range of the polarization curves is set from the open circuit voltage to 0 V, and the scan rate is set as 5 mV•s^{-1}. After obtaining the original polarization curves, tests for obtaining high frequency (20 kHz) resistance are conducted to further remove the ohmic resistances (i.e., contact resistance, resistance from membrane, etc.) within the cell. The iR-corrected polarization curves are obtained through above tests to compare the effectiveness of the four SFFs.

Additionally, hydraulic tests are conducted to compare the resulting pressure drops of the positive/negative electrolyte when it cycles through the cell. Two pressure sensors (Tem-Tech Lab; the testing range corresponding to 0 to 50 psi and an accuracy of ±1% full scale) are connected with the inlet and outlet of the flow cell, respectively, to measure the pressures at these two locations when the electrolyte flows through the cell. And the pressure drop curves under different flow fields are obtained under the flow rates corresponding to 20, 40, 60, and 80 mL•min^{-1}, respectively.

2.3. Computational setups

To get detailed mass transfer information in the flow cell, which is hard to be obtained through the experimental method, a 3-D numerical model for the VRFB flow cell is developed via the COMSOL

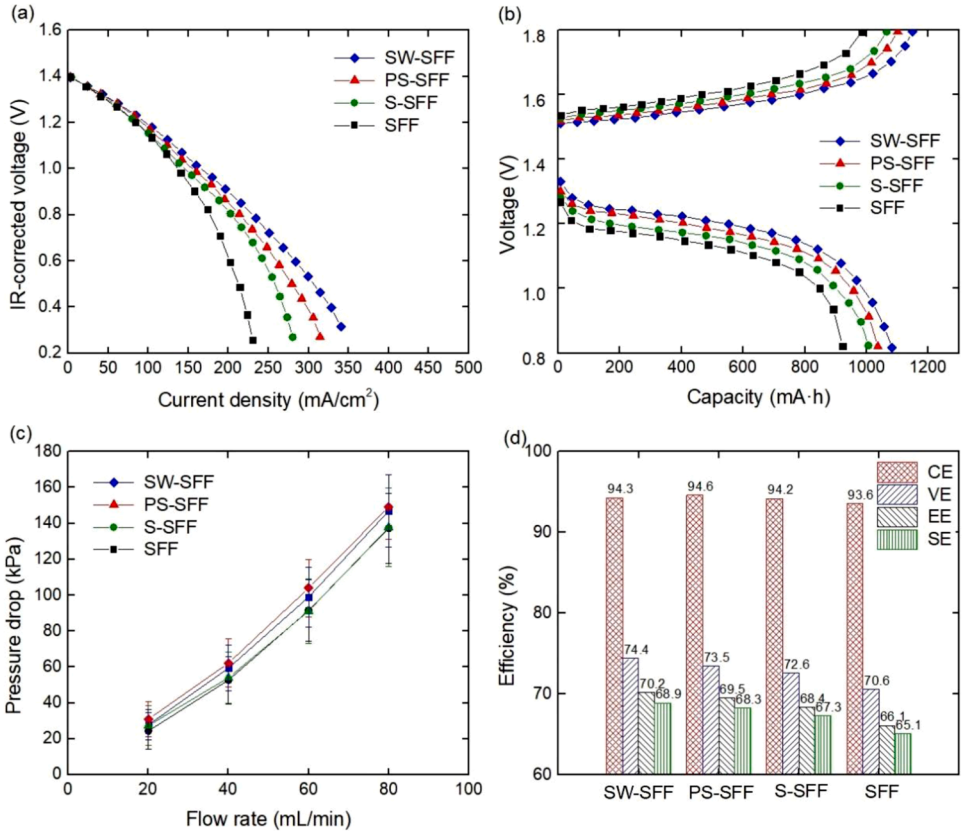

Fig. 2. Electrochemical and hydraulic performance of the VRFB cell implemented with different serpentine flow fields: (a) iR-corrected polarization curves (flow rate corresponding to 30 mL•min^{-1}); (b) charge-discharge curves (current density corresponding to 100 mA•cm^{-2}; flow rate corresponding to 30 mL•min^{-1}); (c) electrolyte pressure drops between the inlet and outlet of the flow cell at varying flow rates; and (d) coulombic efficiencies (CE), voltage efficiencies (VE), and energy efficiencies (EE; pump loss excluded), and system efficiencies of the cell (SE; pump loss included). SFF denotes serpentine flow field; S-SFF denotes serpentine flow field with the sloping channels; PS-SFF denotes serpentine flow field with the partially sloping channels, and SW-SFF denotes serpentine flow field with the stepwise channels. Each electrode consists of five layers of carbon paper. The results were experimentally measured.

Multiphysics® software. The model is built up based on fluid dynamics, mass transfer, and electrochemical reaction parts [8]. The details with respect to the model including the simplifications and assumptions, governing equations, boundary conditions, related electrolyte properties, and electrochemical kinematic parameters are all presented in the former paper [9]. The validation of the numerical model against experimental results is presented in Fig. S2 in *Supplementary Material.* The resulting electrolyte penetration is simulated and calculated for all the four different SFFs. In addition, the distributions of the electrolyte velocity, concentration of reactants, and concentration overpotential in the middle cross-section of the electrode in the in-plane direction are also generated and presented in *Section 3*.

3. Results

To verify the effectiveness of the rib-width-changing SFFs, the resulting polarizations, charge-discharge capacities, pressure drops of the flow cells are obtained experimentally and presented in *Section 3.1*. The resulting overall energy efficiencies of the flow cell under the four SFFs are calculated accordingly and compared vis-à-vis. Then, in *Section 3.2*, based on the computational results, the distributions of the pressure difference, under-the-rib hydraulic resistance, and intra-electrode flow under the four different SFFs are presented. *Section 3.3* further investigates the interactions among multiple U-shaped segments and presents the distributions of the electrolyte penetration and the concentration of reactants along multiple U-shaped segments. Last, the effects of the thickness of the electrode and the applied flow rate on the mass transfer performance of the flow cells with the four different SFFs are compared experimentally and the corresponding results are presented in *Sections 3.4* and *3.5*, respectively.

3.1. Efficiencies based on experiments

The electrochemical and hydraulic performances of the flow cells with the four different SFFs have been investigated via the experimental method. Fig. 2a shows the iR-corrected polarization curves of the VRFB. As shown in Fig. 2a, by adjusting the under-the-rib hydraulic resistance, the limiting current densities obtained by using the proposed modified SFFs are all extended by more than 20% compared to that obtained by using the conventional SFF. Among the three modified SFFs, the one with the stepwise channels (SW-SFF) leads to the highest limiting current density corresponding to approximately 350 mA•cm^{-2}. The possible explanations for the extended limiting current density are provided in *Section 3.2*. Consistent with the polarization results, the proposed SFFs also extend the charge and discharge capacities of the flow cell (Fig. 2b). Regarding the pressure drops resulting from the electrolyte circulation, the PS-SFF and SW-SFF lead to slightly higher pressure drops among the investigated four cases (Fig. 2c), which is possibly due to the increments in the disturbances that are introduced to the bulk electrolyte flow by the partial sloping and the stepwise channels. Nevertheless, the differences in the pressure drops of the four cases are within the range of the measurement errors (Fig. 2c). Overall, the voltage efficiencies of the flow cell with the adjusted SFFs are all increased compared to that with the conventional SFF (Fig. 2d). By taking into account the effect of the pump power on the energy efficiency, the overall system efficiencies are calculated. The experimental results show that the SW-SFF yields the highest system efficiency of 68.9%, approximately an absolute increment of 3.8% compared to that with the conventional SFF. The PS-SFF and S-SFF also lead to increments in the overall system efficiencies. It should be noted that the increments in the overall system efficiencies by using the proposed SFFs are subject to the scale of the flow cell (*Discussion*), the applied flow rate, and the thickness of the electrode (*Sections 3.4* and *3.5*).

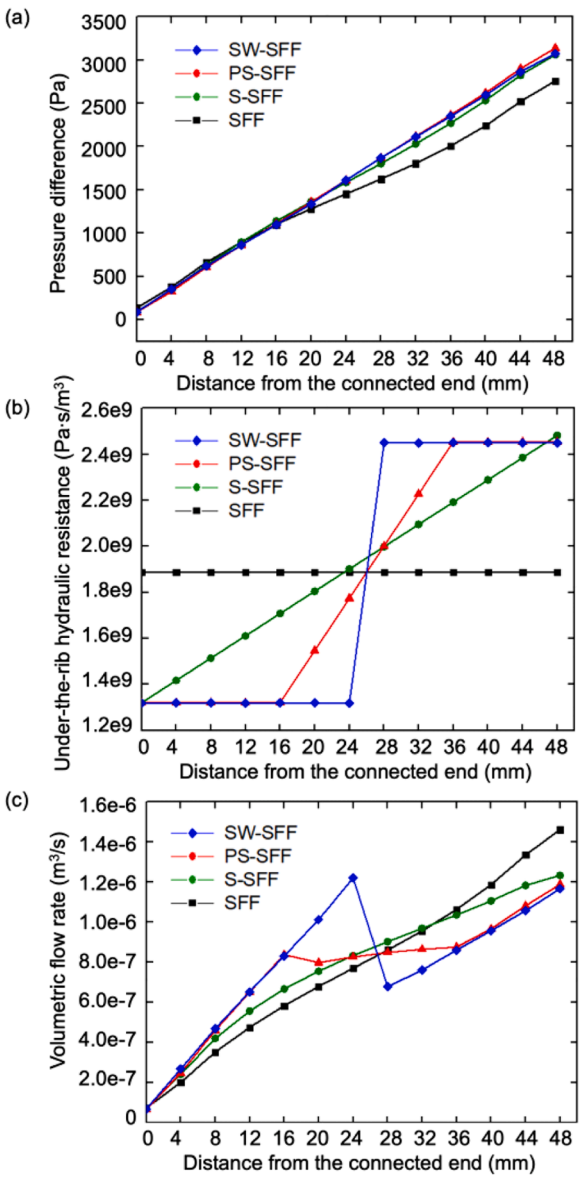

Fig. 3. (a) Pressure difference, (b) under-the-rib hydraulic resistance, and (c) volumetric flow penetrating into the interface between the two central flow passages and the porous electrode (flow rate corresponding to 30 mL•min^{-1} and 5 layers of carbon paper in one electrode). The connected end denotes the conner turn that connects the investigated two flow passages. SFF denotes the conventional serpentine flow field; S-SFF denotes the serpentine flow field with the sloping channels; PS-SFF denotes the serpentine flow field with the partially sloping channels; and SW-SFF denotes the serpentine flow field with the stepwise channels. The results were obtained by simulations.

3.2. Distribution of electrolyte penetration along one U-shaped segment based on simulations

In this section, the pressure differences between two adjacent flow passages are calculated based on the simulated pressure field in the flow cell, which is defined as the pressure difference between two corresponding points at the two ends of one blue dashed line in the SFFs, i.e., flow paths as illustrated in the Fig. 1. The pressure distribution in the whole electrode is shown as Fig. S3 in *Supplementary Material*. Besides, the corresponding under-the-rib hydraulic resistance is defined based on Darcy's law [28]. It describes the hydraulic resistance between the pair of two corresponding points involved in the above definition of the pressure difference. The under-the-rib hydraulic resistance is defined as follow:

$$R = \frac{\nu}{K}\frac{l}{hw} \tag{1}$$

Where, R is the under-the-rib hydraulic resistance; ν is the dynamic viscosity of the electrolyte (3.237×10^{-3} Pa•s for the vanadium-based electrolyte); K is the permeability of the electrode (see Table S1 in *Supplementary Material*); l is the distance between the two ends of the flow path in the electrode (flow paths in the electrode are illustrated by the blue dashed lines in Fig. 1; approximately equals to the sum of the local widths of the rib and channel); h is the thickness of the electrode after compression (*Section 2.2*); and w is the length of one flow passage.

The volumetric flow that penetrates into the interface between two neighboring flow passages and the porous electrode is then determined by dividing the pressure difference by the corresponding hydraulic resistance. As shown in Fig. 3a, the distributions of the calculated pressure differences in the flow cells with different SFFs all show the similar trend that the pressure difference gradually increases from the connected end to the open end of the U-shaped segment, which are consistent with the observations in the previous studies. It should be noted that the pressure differences close to the open end are slightly lower in the cell with the conventional SFF than those in the cells with the adjusted SFFs. This may be a result of the smaller pressure losses along the serpentine channel in the cell with the conventional SFF that has fewer disturbances compared to the adjusted SFFs (especially the PS-SFF and SW-SFF). Fig. 3b shows the distribution of the under-the-rib hydraulic resistance along the U-shaped segment. Under the assumptions that the properties of the electrode and electrolyte such as permeability (see Table S1 in *Supplementary Material*) and viscosity (3.237×10^{-3} Pa•s for the vanadium-based electrolyte) are homogeneous, the under-the-rib hydraulic resistance is proportional to the local width of the rib (Eq. 1). Therefore, the under-the-rib hydraulic resistance stays constant along the whole U-shaped segment in the cell with the conventional SFF that has the constant width of the rib. As a result, from the connected end to the open end of the U-shaped segment, the penetration flow rate increases gradually as the pressure difference rises in the cell with the conventional SFF (see the black line in Fig. 3c).

With the proposed designs for changing the width of the ribs as illustrated in Fig. 1, the under-the-rib hydraulic resistance is changed accordingly as shown in Fig. 3b. Specifically, the under-the-rib hydraulic resistance increases gradually in the cell with the S-SFF or increases in the stepwise manner with the SW-SFF from the connected end to the open end of the U-shaped segment. By modifying the under-the-rib hydraulic resistance to be in concert with the distribution of the pressure difference, the distribution uniformities of the resulting electrolyte penetration along the U-shaped segment in the cells with the modified SFFs are all effectively enhanced (Fig. 3c). Besides, as the volumetric penetration flow rates in the flow cells with the rib-width-charging SFFs first increase and then decrease from the turns that connect the neighboring flow passages to the open end of the U-shaped segment (Fig. 3c). Therefore, overall, the accumulated penetration flow rates along the whole U-shaped segment are similar in the investigated different SFFs.

When the S-SFF is applied, the under-the-rib hydraulic resistance changes gradually along the U-shaped segment (green line in Fig. 3b). As a result, the small hydraulic resistance near the connected end leads to a slight increment in the volumetric flow penetrating into the interface (green line in Fig. 3c). Unlike the S-SFF, when the PS-SFF or SW-SFF is used, the under-the-rib hydraulic resistance is largely reduced along the first part of the U-shaped segment starting from the connected end, and then undergoes a linear change or a stepwise change sharply. Although the significantly enlarged under-the-rib hydraulic resistance near the open end of the U-shaped segment leads to a reduction in the electrolyte penetration as compared to that with the use of the SFF (red and blue lines in Fig. 3b and c), the improvement with respect to the electrolyte penetration near the connected end exceeds the negative impact near the open end. Overall, the SW-SFF induces the largest deviation in the

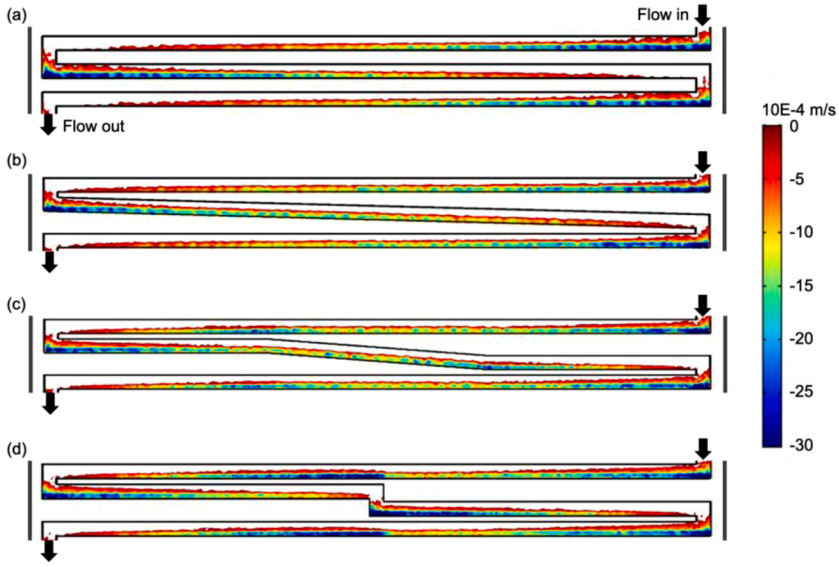

Fig. 4. Distribution of the electrolyte penetration velocity in the through-plane direction at the interface of the electrode and flow field (flow rate corresponding to 30 mL•min^{-1} and five layers of carbon paper in each electrode): (a) conventional serpentine flow field, (b) serpentine flow field with the sloping channels, (c) serpentine flow field with the partially sloping channels, and (d) serpentine flow field with the stepwise channels. Positive velocities showing electrolyte getting out the electrode are not provided. The results were obtained by simulations.

under-the-rib hydraulic resistance from the constant value, followed by the PS-SFF, and the S-SFF leads to the least deviation among the three modified SFFs (Fig. 3b). Under the specific electrode and operation setups, the use of the SW-SFF yields the best penetration distribution of the electrolyte along the U-shaped segment among the four SFFs. As mentioned in *Section 3.1*, the use of the SW-SFF yields the highest voltage and system efficiencies of the cell (Fig. 2d) as well as the highest limiting current density (Fig. 2a). Nevertheless, the results are subject to the magnitude of the under-the-rib hydraulic resistance and operation setups (see *Sections 3.4* and *3.5*).

3.3. Distributions of penetration, velocity, and concentration of reactants based on simulations

To get a full picture of the distribution of the electrolyte flow penetrating into the porous electrode along multiple U-shaped segments, the simulative results at the interface of the flow field (i.e., bipolar plate) and the electrode are generated from the 3-D modeling results. The penetration velocity is described by the velocity component of the electrolyte in the through-plane direction (i.e., in the z direction as shown in Fig. 1). The resulting volumetric flow penetrating into the interface between the flow passages and the electrode is displayed in Fig. 4. The negative velocity values indicate that the electrolyte penetrates into the electrode. The distribution of the positive velocity values that indicate electrolyte getting out of the electrode is illustrated as the blank portion in the under-the-channel area in Fig. 4 to distinguish the penetration in and out behavior.

As shown in Fig. 4a, the penetration velocity increases gradually from the connected end to the open end of each U-shaped segment in the cell with the conventional SFF, which is consistent with the results as shown in Fig. 3c (black line). Compared to the conventional SFF, when the S-SFF is used, the velocities in the through-plane direction near the corner turns are slightly improved, while the velocities far away from the corner turns are slightly decreased (Fig. 4b). The enhancements in the uniformity of the electrolyte penetration are more significant in the cells with the PS-SFF and SW-SFF, owing to the significant variations in the under-the-rib hydraulic resistances as shown in Fig. 3b. It should be noted that Fig. 4 intercepts the middle part of the complete flow field as the distribution trend is generally periodic in the complete flow field, and the integral penetration distribution is provided as Fig. S4 in *Supplementary Material.* Besides, the overall penetration flow rate (estimated by integrating the penetration velocity at the whole interface between the flow field and the porous electrode) and the penetration uniformity

Table 1
Overall penetration flow rate and penetration uniformity of the flow cells implemented with different flow fields.

Flow field	Overall penetration flow rate [m^3/s]	Penetration uniformity[†]
SFF	1.51×10^{-6}	0.12
S-SFF	1.53×10^{-6}	0.14
PS-SFF	1.52×10^{-6}	0.15
SW-SFF	1.55×10^{-6}	0.17

[†] Note that the definition of the penetration uniformity is provided in Supplementary Material.

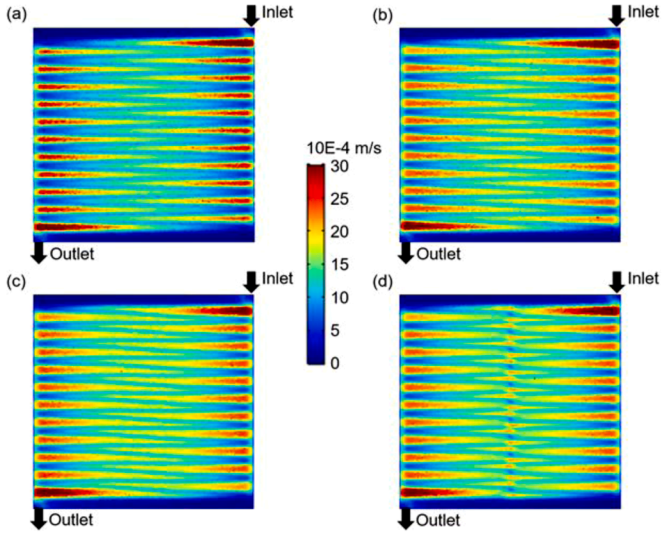

Fig. 5. Electrolyte velocity distribution at the central cross-section of the electrode in the in-plane direction (flow rate corresponding to 30 mL•min^{-1} and five layers of carbon paper in each electrode): (a) conventional serpentine flow field, (b) serpentine flow field with the sloping channels, (c) serpentine flow field with the partially sloping channels, and (d) serpentine flow field with the stepwise channels. The results were obtained by simulations.

of different SFFs are calculated based on the simulated distribution results of the penetration velocity. The performance improvements in the flow cells implemented with the proposed rib-width-changing SFFs are a result of both the increased volumetric flow rate of the electrolyte that

Table 2
Velocity variance at the central cross-section of the electrode in the in-plane direction.

Flow field	Velocity variance [m^2/s^2]	
Electrode surface area [cm × cm]	5 × 5	20 × 20
SFF	1.17×10^{-6}	4.62×10^{-6}
S-SFF	1.10×10^{-6}	4.12×10^{-6}
PS-SFF	9.79×10^{-7}	3.02×10^{-6}
SW-SFF	8.44×10^{-7}	2.21×10^{-6}

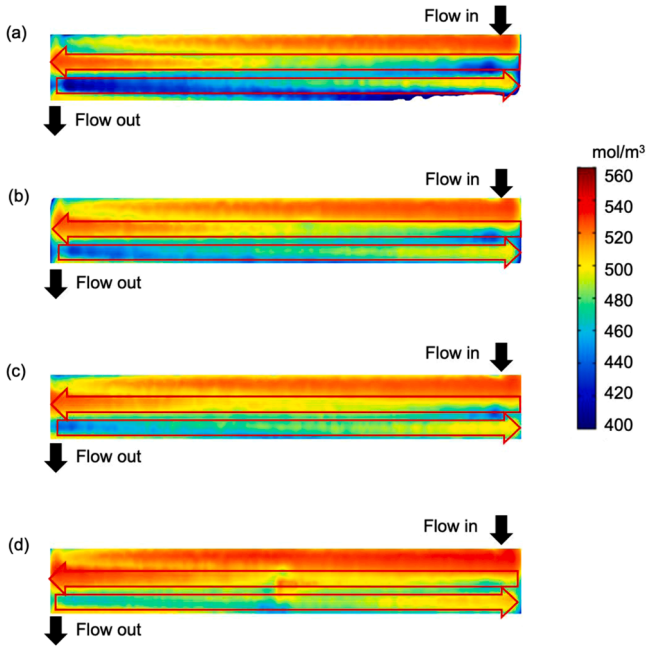

Fig. 6. Concentration distribution of V^{3+} in the in-plane direction at the central cross-section of the electrode (flow rate and current density are 30 mL•min^{-1} and 100 mA•cm^{-2}, respectively; 5 layers of carbon paper in each electrode): (a) conventional serpentine flow field, (b) serpentine flow field with the sloping channel, (c) serpentine flow field with the partially sloping channel, and (d) serpentine flow field with the stepwise channel. The red arrows point from the connected end to the open end of the U-shaped segment. The results were obtained by simulations.

penetrates into the porous electrode and the improved penetration uniformity. As shown in Table 1, the overall penetration flow rates of different flow fields fluctuate in a small range with the largest difference corresponding to approximately 3%. Based on the calculation for the maximum limiting current density of the flow cell with SFF proposed by Ke et al. [25], the 3% increment in the volumetric flow rate corresponds to a 3% increment in the maximum limiting current density. However, it accounts for only a small fraction of the more than 50% improvement in the limiting current density of the flow cell implemented with the SW-SFF as compared to the conventional SFF. By contrast, the penetration uniformities are improved significantly with rib-width-changing SFFs, with the SW-SFF yielding the best penetration uniformity and improving the uniformity to approximately 140% of that under the conventional SFF.

Fig. 5 shows the velocity distribution at the central cross-section of the electrode in the in-plane direction. As the distribution of the electrolyte penetration is changed with the modified SFFs, the in-plane velocities are also altered. Compared to the conventional SFF (Fig. 5a), the distribution uniformities of the in-plane velocities under the modified SFFs (Fig. 5(b-d)) are all elevated. To characterize the improvement, the variance values of the velocity distributions in Fig. 5 are calculated. As shown in Table 2, among the four SFFs, the SW-SFF yields the best uniformity, reducing the variance to approximately 70% of that under the conventional SFF. Besides, the uniformity improvements through the use of the rib-width-changing SFFs are also calculated for relatively large flow cells (e.g., with an active area corresponding to 20 cm × 20 cm), the results are elaborated in *Section 4.1*.

Fig. 6 that intercepts the middle part of the complete electrode, shows the electrolyte concentration distribution of the reactant V^{3+} in the in-plane direction. In the cell with the conventional SFF (Fig. 6a), consistent with the velocity distribution as shown in Fig 5a, the concentration of the reactant V^{3+} gradually increases from the connected end to the open end along each U-shaped segment. While in the cells with the modified SFFs (Fig. 6b-d), the uniformity of the reactants concentration is obviously elevated, especially for the SW-SFF. Besides, as the concentration overpotential is dominated by the distributions of the velocity and reactant's concentration, the modified SFFs reduce the concentration overpotential in the electrode, and the related results are presented in Fig. S5 in *Supplementary Material.*

3.4. Effects of electrode thickness

Given that the thickness of the electrode directly affects the under-the-rib hydraulic resistance (Eq. 1), its effects on the polarization of the flow cell implemented with different SFFs are investigated under the flow rate corresponding to 30 mL•min^{-1}. The thickness of the electrode is varied by using different layers of carbon paper in each electrode. As shown in Fig. 2a, the SW-SFF enhances the limiting current density to the largest extent when five layers of carbon paper is used in each electrode. However, as shown in Fig.7, when the electrode thickness is relatively small (e.g., one layer or three layers of carbon paper in each electrode), the PS-SFF outperforms the S-SFF and SW-SFF. The SW-SFF yields the least limiting current density among the three modified

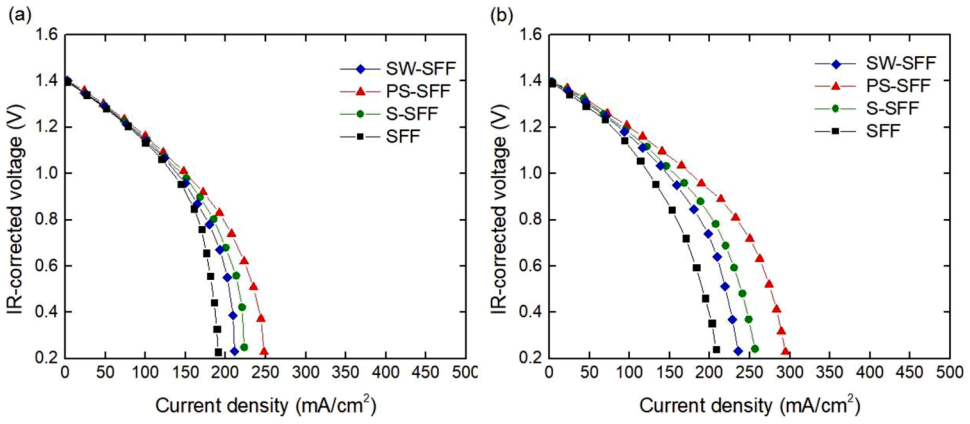

Fig. 7. IR-corrected polarization curves with (a) one-layer and (b) three-layer carbon paper in each electrode (flow rate corresponding to 30 mL•min^{-1}). The results obtained with the five-layer carbon paper electrodes are provided in Fig. 2. SFF denotes the conventional serpentine flow field; S-SFF denotes the serpentine flow field with the sloping channels; PS-SFF denotes the serpentine flow field with the partially sloping channels; and SW-SFF denotes the serpentine flow field with the stepwise channels. The results were experimentally measured.

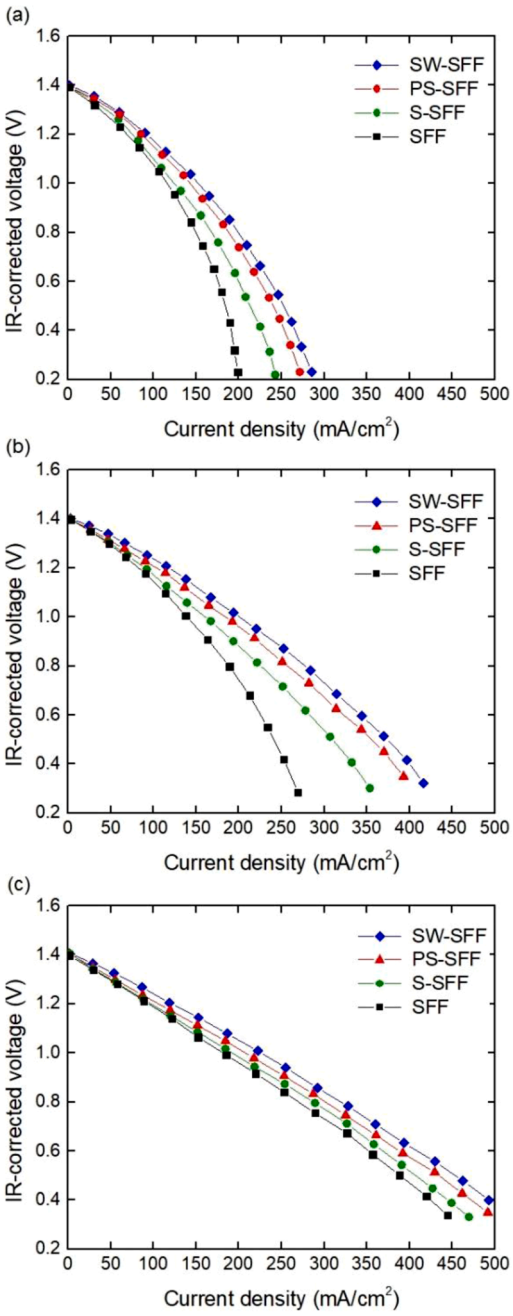

Fig. 8. IR-corrected polarization curves with five-layer carbon paper being used in each electrode at the applied flow rate corresponding to: (a) 20 mL•min^{-1}; (b) 40 mL•min^{-1}; and (c) 50 mL•min^{-1}. SFF denotes the conventional serpentine flow field; S-SFF denotes the serpentine flow field with the sloping channel; PS-SFF denotes the serpentine flow field with the partially sloping channel; and SW-SFF denotes the serpentine flow field with the stepwise channel. The results were experimentally measured.

SFFs in Fig. 7a and b. It is hypothesized that the large deviation from the constant width of the ribs such as achieved by using the SW-SFF favors relatively high under-the-rib hydraulic resistance (e.g., when five-layer carbon paper is used in each electrode; see results in Fig. 2a). When a thin electrode is used (such as one-layer or three-layer carbon paper; see results in Fig. 7), the under-the-rib flow resistance in the second half part of the U-shaped segment near the open end increases dramatically. Once the negative effects of the second half part exceed the positive effects of the first half part, the performance of the flow cell with the SW-SFF gets worse. In addition, the higher limiting current density enabled by the PS-SFF compared to the S-SFF is hypothetically owing to the additional disturbance induced by the PS-SFF (*Section 3.1*).

3.5. Effects of flow rate

The effects of the applied flow rate on the polarization of the flow cells with the four SFFs are also experimentally explored. Results show that the modified SFFs effectively enhance the mass transfer under the flow rates less than 50 mL•min^{-1} (see Fig. 8a-8b and 2a). Under the flow rate corresponding to 50 mL•min^{-1} (Fig. 8c), there are no sharp drops in the polarization curves. When the polarization is less limited by the concentration overpotential, the differences in the four polarization curves under the four SFFs are largely reduced as shown in Fig. 8c.

4. Discussion

4.1. Implication for large-scale flow cell

It has been found in the previous studies that the nonuniform mass transfer becomes a leading barrier for a high limiting current density especially in large-scale flow cells [6,9]. Therefore, in this section, the implication of the proposed S-SFF, PS-SFF, and SW-SFF for the large-scale cell (the electrode area corresponding to 20 cm × 20 cm) is investigated. The geometric parameters of the channels and ribs are kept the same as the ones in the lab-scale flow cell (the electrode area corresponding to 5 cm × 5 cm in the present study). Detailed parameters are shown in Table S4 in *Supplementary Material*. The flow rate applied to the large-scale flow cell is proportional with the electrode area to guarantee the constant flow rate supply per electrode area (480 mL•min^{-1} of the large-scale flow cell corresponding to the 30 mL•min^{-1} of the lab-scale flow cell). Based on the simulation results, the velocity variances at the central cross-section of the electrode in the in-plane direction in the large-scale cells with different SFFs are presented in Table 2.

Compared to the lab-scale flow cell, the velocity variances in the large-scale flow cell implemented with different SFFs are significantly higher. Considering that the distribution of the electrolyte penetration is less uniform along the U-shaped segment in the large-scale cell compared to that in the small-scale cell, the proposed S-SFF, PS-SFF, and SW-SFF are expected to enhance the mass transfer to a greater extent in the large-scale cell than in the small-scale cell. As shown in Table 2, the SW-SFF in the large-scale flow cell reduces the velocity variance to 47% of that with the conventional SFF, while in the lab-scale cell, the value is reduced to 70% of that with the conventional SFF.

4.2. Future work

Although the results indicate that the proposed SFFs with the sloping/partial sloping/stepwise channel outperforms the conventional SFF from different aspects as shown in *Sections 3* and *4.1*, there are a few further improvements that should be examined in the future work. First, the impacts of the geometric parameters of the modified SFFs should be further explored. An optimization model or a design guidance is beneficial for the further improvements in the mass transfer capability and uniformity in the flow cell with the SFF designs. In addition, considering that the relatively large pump loss is a critical barrier in practical applications of RFBs, the proposed SFF designs should be further modified, such as by smoothing bending points or width-changing points of the ribs, to avoid large pump losses. Last, the experiments in the present study were conducted on the VRFB cell with the active area corresponding to 5 cm × 5 cm that is significantly smaller than the typically area used in practical applications. Further experiments should be conducted on the large-scale flow cells for verifying the performance of the rib-width-changing SFFs.

5. Conclusions

In the present study, three different modified SFFs are proposed for making the under-the-rib hydraulic resistance in concert with the pressure difference distribution along U-shaped segments, including SFF with the sloping channel, SFF with the partially sloping channel, and SFF with the stepwise channel. Main findings of the present study via the computational and experimental methods are as follows:

- The electrolyte penetration uniformity along the U-shaped segments is effectively enhanced by using the modified SFFs: the limiting current density of the small-scale flow cell (active area corresponding to 5 cm × 5 cm) is improved by up to 60% of that of the flow cell with the conventional SFF. And the energy efficiency (pump power consumption included) is increased by approximately 4% under the applied current density and flow rate corresponding to 100 $mA \cdot cm^{-2}$ and 30 $mL \cdot min^{-1}$, respectively. In addition, the impacts of the modified SFFs on the electrolyte penetration uniformity is expected to be more significant in large-scale flow cells, such as the cell with an active area corresponding to 20 cm × 20 cm.
- Among the three modified SFFs, the SW-SFF yields the highest limiting current density when five layers of carbon paper is used in each electrode while the PS-SFF yields the best performance when the thin electrode is used. The effectiveness of the modified SFFs is subject to the magnitude of the under-the-rib hydraulic resistance and the applied flow rate.

CRediT authorship contribution statement

Jie Sun: Conceptualization, Methodology, Data curation, Writing – original draft. **Baichen Liu:** Validation, Investigation, Writing – original draft. **Menglian Zheng:** Supervision, Funding acquisition, Writing – review & editing. **Yansong Luo:** Investigation. **Zitao Yu:** Supervision.

Declaration of Competing Interest

None

Acknowledgments

This work was supported by the National Natural Science Foundation of China [no. 51606164].

Supplementary materials

Supplementary material associated with this article can be found, in the online version, at doi:10.1016/j.est.2022.104135.

References

[1] N. Kittner, F. Lill, D.M. Kammen, Energy storage deployment and innovation for the clean energy transition, Nat. Energy 2 (2017), 2017125.
[2] P. Alotto, M Guarnieri, F Moro, Redox flow batteries for the storage of renewable energy: a review, Renew. Sustain. Energy Rev. 29 (2014) 325–335.
[3] North American Electric Reliability Corporation, 2013 Long-term Reliability Assessment, 2013. http://www.nerc.com/pa/RAPA/ra/Reliability%20Assessments%20DL/2013_LTRA_FINAL.pdf.
[4] P. Leung, X. Li, P.D.L. Carlos, L. Berlouis, C.T.J. Low, F.C. Walsh, Progress in redox flow batteries, remaining challenges and their applications in energy storage, RSC Adv. 2 (27) (2012) 10125–10156.
[5] A. Bhattarai, N. Wai, R. Schweiss, A. Whitehead, G.G. Scherer, P.C. Ghimire, T. M. Lim, H.H. Hng, Vanadium redox flow battery with slotted porous electrodes and automatic rebalancing demonstrated on a 1 kW system level, Appl. Energy 236 (2019) 437–443.
[6] R. Gundlapalli, S. Jayanti, Effective splitting of serpentine flow field for applications in large-scale flow batteries, J. Power Source. 487 (2021), 229409.
[7] J. Sun, M.L. Zheng, Y.S. Luo, Z.T. Yu, Three-dimensional detached serpentine flow field design for redox flow batteries, J. Power Source. 428 (2019) 136–145.
[8] Q. Xu, T.S. Zhao, P.K. Leung, Numerical investigations of flow field designs for vanadium redox flow batteries, Appl. Energy 105 (2013) 47–56.
[9] J. Sun, M.L. Zheng, Z.S. Yang, Z.T. Yu, Flow field design pathways from lab-scale toward large-scale flow batteries, Energy 173 (2019) 637–646.
[10] M.L. Zheng, J. Sun, M. Christoph, T. Wang, Pathways toward enhanced techno-economic performance of flow battery systems in energy system applications, J. Electrochem. Energy Convers. 16 (2) (2018), 021001.
[11] X.L. Zhou, T.S. Zhao, L. An, Y.K. Zeng, L. Wei, Critical transport issues for improving the performance of aqueous redox flow batteries, J. Power Source. 339 (2017) 1–12.
[12] Y.K. Zeng, X.L. Zhou, L. An, L. Wei, T.S. Zhao, A high-performance flow-field structured iron-chromium redox flow battery, J. Power Source. 324 (2016) 738–744.
[13] X.L. Zhou, L.Y. Yun, Y.H. Lv, X.Y. Zhang, L.D. Fan, Q.X. Wu, Elucidating effects of component materials and flow fields on Sn–Fe hybrid flow battery performance, J. Power Source. 450 (2020), 227613.
[14] D. Zhong, R. Lin, D.C. Liu, X. Cai, Structure optimization of anode parallel flow field for local starvation of proton exchange membrane fuel cell, J. Power Source. 403 (2018) 1–10.
[15] E. Alizadeh, M. Rahimi-Esbo, S.M. Rahgoshay, S.H.M. Saadat, M. Khorshidian, Numerical and experimental investigation of cascade type serpentine flow field of reactant gases for improving performance of PEM fuel cell, J. Power Source. 42 (21) (2017) 14708–14724.
[16] L. Wan, H.T. Liu, Performance studies of PEM fuel cells with interdigitated flow fields, J. Power Source. 134 (2) (2004) 185–196.
[17] M. Lu, Y. Jiao, X. Tang, W. Yang, M. Ye, Q. Xu, Blocked serpentine flow field with enhanced species transport and improved flow distribution for vanadium redox flow battery, J. Energy Storage 35 (1) (2021), 102284.
[18] R. Gundlapalli, S. Jayanti, Effect of electrolyte convection velocity in the electrode on the performance of vanadium redox flow battery cells with serpentine flow fields, J. Energy Storage 30 (2020), 101516.
[19] Q. Wang, Z.G. Qu, Z.Y. Jiang, W.W. Yang, Numerical study on vanadium redox flow battery performance with non-uniformly compressed electrode and serpentine flow field, Appl. Energy 220 (15) (2018) 106–116.
[20] M. Macdonald, R.M. Darling, Comparing velocities and pressures in redox flow batteries with interdigitated and serpentine channels, AlChE J. (2019), https://doi.org/10.1002/aic.16553.
[21] S. Kumar, S. Jayanti, Effect of flow field on the performance of an all-vanadium redox flow battery, J. Power Source. 307 (2016) 782–787.
[22] M.Y. Lu, Y.H. Jiao, X.Y. Tang, X.Y. Tang, M. Ye, Q. Xu, Blocked serpentine flow field with enhanced species transport and improved flow distribution for vanadium redox flow battery, J. Power Source. 35 (2021), 102284.
[23] X.Y. Ke, J.M. Prahl, J.I.D. Alexander, R.F. Savinell, A simple analytical model of coupled single flow channel over porous electrode in vanadium redox flow battery with serpentine flow channel, J. Power Source. 288 (2015) 308–313.
[24] X.Y. Zhang, X. Zhang, H. Taira, H. Liu, Error of Darcy's law for serpentine flow fields: An analytical approach, Int. J. Hydrog. Energy 43 (2018) 6686–6695.
[25] X.Y. Ke, J.M. Prahl, J.I.D. Alexander, R.F. Savinell, Redox flow batteries with serpentine flow fields: Distributions of electrolyte flow reactant penetration into the porous carbon electrodes and effects on performance, J. Power Source. (2018) 295–302.
[26] X.Y. Ke, J.M. Prahl, J.I.D. Alexander, R.F. Savinell, Flow distribution and maximum current density studies in redox flow batteries with a single passage of the serpentine flow channel, J. Power Source. 270 (2014) 646–657.
[27] J. Houser, J. Clement, A. Pezeshki, M.M. Mench, Influence of architecture and material properties on vanadium redox flow battery performance, J. Power Source. 302 (2016) 369–377.
[28] S. Maurya, P.T. Nguyen, Y.S. Kim, Q. Kang, R. Mukundan, Effect of flow field geometry on operating current density, capacity and performance of vanadium redox flow battery, J. Power Source. 404 (2018) 20–27.
[29] J.T. Clement, T.A. Zawodzinski, M.M. Mench, Measurement of localized current distribution in a vanadium redox flow battery, ECS Trans. 58 (37) (2014) 9–16.
[30] B.C. Liu, M.L. Zheng, J. Sun, Z.T. Yu, No-mixing design of vanadium redox flow battery for enhanced effective energy capacity, J. Energy Storage 23 (2019) 278–291.